Journal of the Mechanical Behavior of Biomedical Materials 74 (2017) 371–382

Contents lists available at ScienceDirect

Journal of the Mechanical Behavior of Biomedical Materials

journal homepage: www.elsevier.com/locate/jmbbm

The micro-damage process zone during transverse cortical bone fracture: No ears at crack growth initiation

Thomas Willett[a,c,*], David Josey[b], Rick Xing Ze Lu[b], Gagan Minhas[b], John Montesano[c]

[a] Systems Design Engineering, Biomedical Engineering Program, University of Waterloo, Waterloo, Ontario, Canada
[b] Nanotechnology Engineering, University of Waterloo, Waterloo, Ontario, Canada
[c] Mechanical and Mechatronics Engineering, University of Waterloo, Ontario, Canada

ARTICLE INFO

Keywords:
Cortical bone
Fracture toughness
J-integral
Micro-damage
Micro computed tomography
Process zone

ABSTRACT

Objective: Apply high-resolution benchtop micro-computed tomography (micro-CT) to gain greater understanding and knowledge of the formation of the micro-damage process zone formed during traverse fracture of cortical bone.

Methods: Bovine cortical bone was cut into single edge notch (bending) fracture testing specimens with the crack on the transverse plane and oriented to grow in the circumferential direction. We used a multi-specimen technique and deformed the specimens to various individual secant modulus loss levels (P-values) up to and including maximum load (Pmax). Next, the specimens were infiltrated with a $BaSO_4$ precipitation stain and scanned at 3.57-μm isotropic voxel size using a benchtop high resolution-micro-CT. Measurements of the micro-damage process zone volume, width and height were made. These were compared with the simple Irwin's process zone model and with finite element models. Electron and confocal microscopy confirmed the formation of $BaSO_4$ precipitate in micro-cracks and other porosity, and an interesting novel mechanism similar to tunneling.

Results: Measurable micro-damage was detected at low P values and the volume of the process zone increased according to a second order polynomial trend. Both width and height grew linearly up to Pmax, at which point the process zone cross-section (perpendicular to the plane of the crack) was almost circular on average with a radius of approximately 550 μm (approximately one quarter of the unbroken ligament thickness) and corresponding to the shape expected for a biological composite under plane stress conditions.

Conclusion: This study reports details of the micro-damage fracture process zone previously unreported for cortical bone. High-resolution micro-CT enables 3D visualization and measurement of the process zone and confirmation that the crack front edge and process zone are affected by microstructure. It is clear that the process zone for the specimens studied grows to be meaningfully large, confirming the need for the J-integral approach and it does not achieve steady state at Pmax in most specimens. With further development, this approach may become valuable towards better understanding the role of the process zone in cortical bone fracture and the effects of relevant modifications towards changes in fracture toughness in a cost effective way.

1. Introduction

The study of cortical bone fracture mechanics is widely understood to be critical towards better understanding skeletal fragility, fracture prediction and prevention, and the development of new therapeutics (Martin et al., 2015). Over the last couple of decades, significant work has been done to appropriately measure cortical bone fracture toughness and to understand the complex mechanisms that toughen bone and, conversely, lead to its fragility. In recent years, Robert Ritchie's group at UC Berkeley has highlighted the importance of using the non-linear fracture mechanics J-integral approach (Yang et al., 2006) and on including the R-curve behavior in experimental studies of cortical bone quality and the like (Nalla et al., 2005; Zimmermann et al., 2011). The J-integral approach is promoted for cortical bone because linear elastic fracture mechanic theory does not hold due to the fact that a non-negligible process zone of "plastic" deformation occurs around the crack tip and meaningful non-linear behavior is also noted during testing, particularly for transverse fracture (Martin et al., 2015; Woodside and Willett, 2016; Yan et al., 2007; Yang et al., 2006).

Cortical bone recruits multiple mechanisms to inhibit crack growth

* Corresponding author at: Systems Design Engineering, University of Waterloo, Waterloo, Ontario, Canada.
E-mail address: thomas.willett@uwaterloo.ca (T. Willett).

http://dx.doi.org/10.1016/j.jmbbm.2017.06.029
Received 18 March 2017; Received in revised form 19 June 2017; Accepted 22 June 2017
Available online 24 June 2017

(Launey et al., 2010). The relative importance of each of the toughening mechanisms is somewhat debated (Launey et al., 2010; Nalla et al., 2005; Ritchie et al., 2005). Take micro-crack and micro-damage formation as a specific example (Launey et al., 2010; Nalla et al., 2004; Vashishth et al., 2003). During cortical bone fracture, the phenomenon termed "constrained micro-cracking" occurs in the process zone ahead of the crack tip both before crack propagation (i.e. it is an intrinsic toughening mechanism) and, as the crack grows, a field of "constrained micro-cracking" is left in the wake (Launey et al., 2010; Nalla et al., 2004; Vashishth et al., 2003). This form of micro-cracking has a finer, more diffuse morphology (Poundarik et al., 2012; Poundarik and Vashishth, 2015; Sun et al., 2010) than the classic Frost-Burr micro-cracking, which has been intensely studied over the last several decades (Donahue and Galley, 2006; Taylor and Lee, 2003). This finer diffuse micro-cracking (herein furthermore referred to as 'micro-damage') is much smaller in scale, with lengths on the order of microns rather than the hundreds of μm reported for the Frost-Burr type (Poundarik et al., 2012). Both forms of micro-cracking can be formed in vivo and in vitro, but micro-damage may be the precursor to the larger micro-cracks and indeed fracture. It is associated with the apparent "yielding" of bone under tension in the longitudinal direction (Poundarik et al., 2012; Poundarik and Vashishth, 2015). It is thought to occur as mineralized collagen fibrils are stretched and small-scale fractures nucleate in the mineral phase (Poundarik et al., 2012; Poundarik and Vashishth, 2015). Many suspect, and some evidence supports, the idea that the collagen and other organics and their interface with the mineral phase contribute to controlling the micro-damage (Burton et al., 2014). While cracking of the hydroxyapatite-like mineral phase alone may not absorb much energy (Nalla et al., 2004), it is currently widely thought, though not entirely proven, that the accompanying deformation of the bone collagen (Gupta et al., 2006), and perhaps other organics such as the non-collagenous proteins (Poundarik et al., 2012), and even their debonding from the mineral (Gupta et al., 2007) absorb a significant amount of strain energy (Nalla et al., 2004).

The contribution of micro-damage formation in the process zone to fracture toughness depends on the size and shape of the process zone and the mechanisms that engage upon formation of the diffuse micro-damage within the process zone (Anderson, 2005; Launey et al., 2010). We know very little about these mechanisms, and, to date, the size and shape have been largely assumed based on general predictions from linear elastic fracture mechanics and simpler materials (Martin et al., 2015). A recent textbook portrays the zone as consisting of symmetrical "ears" that form on either side of the crack propagation direction (Martin et al., 2015).

This manuscript reports the results from our first attempts to study the micro-damage process zone in bovine cortical bone specimens undergoing transverse-circumferential fracture in Mode-I. The single edge notch bending configuration and high resolution micro-computed x-ray tomography (HR-micro-CT) combined with a $BaSO_4$ contrast agent were used. The aim was to increase our understanding of this important process in cortical bone fracture in order to improve the mechanistic study of skeletal fragility and the fidelity of computational modeling of cortical bone fracture.

2. Material and methods

Conveniently, the formation of diffuse micro-damage within the process zone enables the visualization and quantification of its dimensions. In the past decade or so, a few studies have reported using micro-CT with heavy metal stain contrast enhancement to study the accumulation of micro-cracking and micro-damage resulting from mechanical loading in bone specimens. (Tang and Vashishth, 2010) used lead uranyl acetate to study micro-cracks in trabecular bone. More recently, a more benign barium sulfate precipitation stain has found application in studies of cortical bone under quasi-static and fatigue loading in compression, tensile and even fatigue of notched bending specimens (Landrigan et al., 2011, 2010; Leng et al., 2008; Turnbull et al., 2011). Recently, (Choudhari et al., 2016) used the barium sulfate approach to study micro-damage formation in the vertebrae of tumorous spines from a rat model exposed to in vitro loading.

The studies mentioned above inspired the development of our own barium sulfate-based, contrast-enhanced, high-resolution micro-CT technique. We have used the technique to study the diffuse micro-damage within the fracture process zone of elastic-plastic fracture mechanics (J_{Ic}) qualified single edge notched bending fracture of cortical bone specimens undergoing Mode-I transverse plane-circumferentially directed fracture. We sought 3-D qualitative characterization and quantification of the dimensions of the process zone as the process zone developed up to and including crack growth initiation.

2.1. Specimen production

Consistent with our previous works, cortical bone was sourced from five tibiae of bovine steers (aged 1.5 – 2 years old) obtained immediately after slaughter from a local abattoir and processed as follows (Burton et al., 2014; Willett et al., 2015; Woodside and Willett, 2016). Steer bone is a useful model when developing new approaches, as in this project, because the bone is relatively more homogeneous, denser, and less porous than typical human cadaveric specimens. The bone was kept frozen (−20 °C) for up to 10 days following sourcing. Bones were thawed and stripped of all soft tissue. Using a morgue band saw, each tibiae was cut into two blocks approximately 70 mm × 25 mm × 6 mm; one mid-diaphysis anterior block and one mid-diaphysis posterior block. Each block was cut into four rectangular beams using an Isomet 1000 diamond wafer saw (Buehler Canada, Whitby, ON, Canada). The length was oriented along the longitudinal direction and the width in the radial direction. Beams were 60 mm × 4 mm × 4 mm (l × w × t). The endosteal side of the beam was marked to track orientation. The bone beams were ground and polished by hand to a 1-μm finish. Beams were stored at −20 °C while wrapped in saline soaked gauze.

The beams were prepared for single-edge notched bend (SEN(B)) fracture testing in three-point bending complying as closely as possible with requirements drawn from ASTM E1820 and ASTM D6068 and consistent with previous studies (Burton et al., 2014; Willett et al., 2015; Woodside and Willett, 2016; Yan et al., 2007). The beams were thawed to room temperature and a starter notch was cut to a depth of 1.9 mm at mid-span into one face in the circumferential direction on the transverse plane using a 300-μm diameter diamond wire saw (Delaware Diamond Knives, Wilmington, DE, USA). Orienting the starter notch in this way meant that the crack would propagate across any osteons, which run longitudinally, if present in the tissue.

Each crack was propagated in the circumferential direction in this study because less severe crack deflections occur relative to the radial direction where the cracks interact with lamellar interfaces and can deflect up to 90°. Thus, avoiding crack deflections simplified later measurements of the micro-damaged process zone. To further avoid severe crack deflections, side grooves aided in maintaining crack propagation direction on the transverse plane, which corresponds to the peak drive force. In previous work, specimens without side-grooves demonstrated significant deflections and crack branching (Woodside and Willett, 2016). Furthermore, side grooves promote a tri-axial ("plane strain") stress state (Anderson, 2005). Rounded side grooves (300-μm wide and 400-μm deep) were cut with the same 300-μm diameter diamond wire saw.

The starter notch was sharpened using an ultra-fine razor blade (McMaster-Carr, Elmhurst, IL, USA) lubricated with 1-μm diamond slurry (Buehler) to produce a total starter notch length of approximately 2 mm and ~ 5-μm tip radius (Burton et al., 2014; Willett et al., 2015; Woodside and Willett, 2016; Yan et al., 2007). While consistent with ASTM D6068, sharpening with a razor blade was also necessary because we have found that starter cracks induced from a blunt notch using fatigue loading deflect almost immediately due to the anisotropy of the

microstructure.

2.2. Mechanical testing

After four hours of soaking in PBS at room temperature to ensure hydration levels, specimen thickness and width were measured with a micrometer (0–25.4 mm digital micrometer (± 4 μm uncertainty), Mitutoyo, Mississauga, ON) and recorded before the specimens were tested using an Instron ElectroPuls E1000 mechanical testing machine (Instron, Norwood, MA, USA). Each specimen was placed notch-side towards the span of a three-point bending jig (two cylindrical supports (diameter 6.35 mm) separated by a span of 40 mm) with the notch and side groves aligned with the load-line, opposite a 6.35 mm diameter cylindrical loading nose. The tests were run under load-line displacement control at 0.5 mm/min. The applied load was measured using a 100 N load-cell (+/−0.5% accuracy). Load-line displacement (deflection of the SEN(B) specimen) was measured using an internal digital linear encoder with sub-micron accuracy and resolution.

In order to enable imaging of the process zone progression up to crack growth initiation, individual beams were randomly selected from the batch of twenty and assigned to one of four groups corresponding to a loading condition: P0 = elastic, reversible loading, P5 = approximately a 5% loss of secant stiffness, P10 = approximately 10% loss of secant stiffness and Pmax, which corresponds to a zero slope of the load versus load-line deflection curve and approximates the advent of crack growth initiation. The use of this P% index originates from linear elastic fracture mechanics in which crack growth initiation is often presumed to have occurred upon an X% loss in secant modulus, where X is typically 5 (Anderson, 2005). Note that this P is not the same as the statistical p-value.

The Pmax specimens were tested first because the zero slope at maximum load point was easily detected during testing. Then the applied load versus load-line deflection curves from this group were averaged and the load-line displacements corresponding to the elastic range (P0), five percent loss of secant modulus (P5) and ten percent loss of secant modulus (P10) were determined (Fig. 2). Then the specimens in each group were tested up to their assigned deflections and unloaded. Inevitably, due to variations between specimens, the actual % loss of secant modulus at the assigned deflection varied around the assigned value. This resulted in a convenient spread of data points, which enabled broader characterization of the process zone formation and growth (See Section 4.3).

2.3. Micro-damage staining

To facilitate detection of the micro-damaged process zone, the fracture specimens were stained using a two-step barium sulfate precipitation staining technique similar to the method reported by (Leng et al., 2008). Barium ions were diffused into the damaged regions by soaking the specimens for three days under vacuum (~ 175 mmHg) in 14 mL of two parts 0.5 M BaCl in ddH_2O and one part acetone, followed by the diffusion of sulfate ions into the damaged regions by soaking the specimens in 14 mL of two parts 0.25 M $NaSO_4$ in ddH_2O and one part acetone, again while under vacuum for three days. The barium and sulfate ions react, staining the micro-damage and various small structures with a dense, insoluble barium sulfate precipitate. Subsequently, each specimen was rinsed with ddH2O to remove any residual free ions.

The composition and distribution of the $BaSO_4$ deposits were confirmed in pilot studies using scanning electron microscopy (SEM) with a back scattered electron detector and energy dispersive x-ray spectroscopy (EDX). An SEM (XL30 ESEM, Philips, USA) was used to image each fracture surface at an accelerating voltage of 20.0 kV and a working distance of 15 mm using a back-scattered electron detector (FEI, Hillsboro, OR, USA). Energy dispersive X-ray spectroscopy (EDAX, SUTW PV7760/77, USA) was used to confirm that the precipitate found in the damaged regions was indeed barium sulfate.

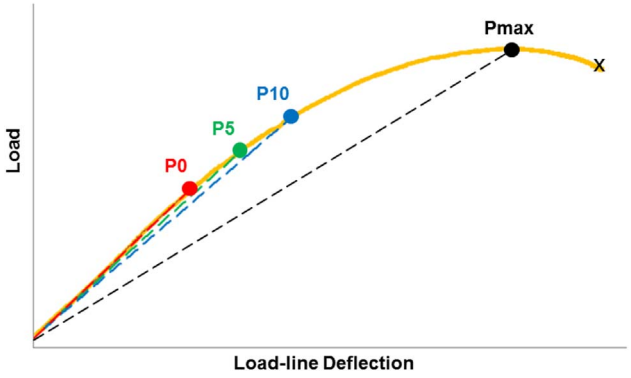

Fig. 1. A model load versus load-line displacement curve demonstrating the scheme for establishing P0, P5, P10 and Pmax based on secant stiffness (dashed lines).

2.4. Micro-CT scanning and reconstruction

Specimens were mounted in a polymer centrifuge tube using low melting point agarose gel (Sigma-Aldrich). A Bruker SkyScan 1172 high resolution X-ray micro-CT (Bruker micro-CT, Billerica, MA, USA) was used to image each specimen (3.57 μm voxel size, 59 kVp, 159 μA current, 3300 ms exposure, 0.2° rotational steps, three frames averaged). All specimens were scanned using the same settings. Reconstructions were performed with Skyscan NRecon software (v. 1.6.8.0, Bruker micro-CT, Billerica, MA, USA). Reconstructions settings included: Gaussian Smoothing = 1, Ring Artifact Correction = 20, Undersampling factor = 1, Threshold for defect pixel mask (%) = 50, Beam Hardening Correction (%) = 60 (Fig. 1).

2.5. Generation of image data sets

For each scan, a region of interest (ROI) originating at the crack tip and of constant dimensions large enough to contain the largest process zone observed in the study (see Fig. 3A) was selected using CTan software (Bruker micro-CT, Billerica, MA, USA) and then exported to DataViewer software (Bruker micro-CT, Billerica, MA, USA). In DataViewer, each dataset was realigned on an orthogonal (X-Y-Z) set of axes with the leading edge of the crack tip parallel to the X axis and direction of maximum driving force (bone circumferential direction) parallel to the Y-axis. This resulted in the transverse fracture plane parallel to the

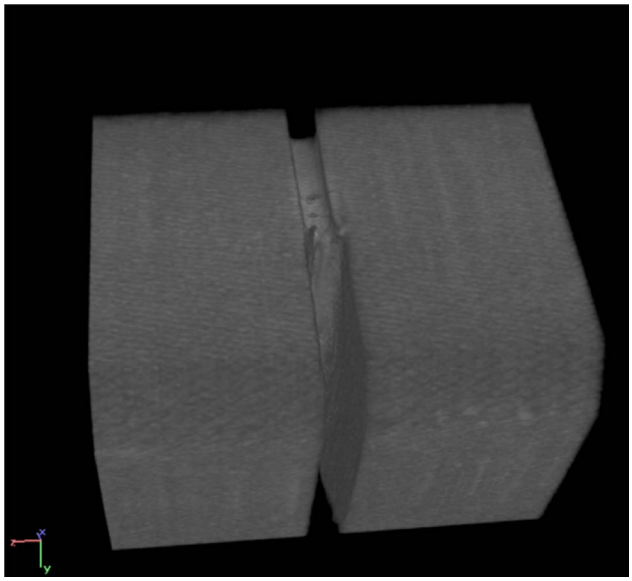

Fig. 2. Example image of a reconstructed micro-CT scan demonstrating the notch and side grooves, which were cut using a diamond wire saw.

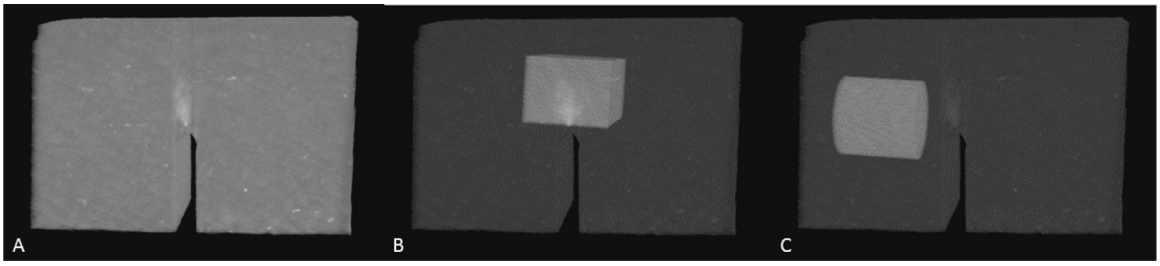

Fig. 3. A) Crack region of interest. B) Crack tip region of interest. C) Cylindrical control region of interest.

X-Y plane. The Z-axis aligned with the length of the beam, which was aligned with the longitudinal direction of the diaphysis during beam cutting procedures.

2.5.1. Image data sets for quantification

For process zone quantification, the realigned datasets were reopened in CTan and a new rectangular region of interest (crack tip ROI; Fig. 3B) centered at the crack tip was defined with faces defined with the X-Y-Z axes as normal vectors. This region of interest was exported as a series of Y-Z plane images stacked in the X-axis and imported into MatLab (Mathworks, Natick, MA, USA, version 2013a) for further image analysis and calculations using custom written code.

2.5.2. Thresholding for BaSO4 stained micro-damage

In order to determine an objective attenuation coefficient threshold for segmenting the micro-damage from the surrounding bone in each specimen, a cylindrical control ROI, with a radius of 0.65 mm and a length of 0.66 mm, was taken from an undamaged region of each scan distal from the crack tip and at the center of the specimen (X-Y plane). This is a region where loading, damage and surface over-staining are known to be negligible. See Fig. 3C for reference. An attenuation coefficient histogram from each control ROI was generated and then the threshold above which only 1% of the pixels remained was determined (Burton et al., 2014). The value of this threshold varied minimally between specimens. Once applied to the paired crack tip ROI, the approach allowed reduction of non-specific staining noise due to varying porosity and other uncontrolled variables. In CTan, pseudo-colored images of each process zone (on the Y-Z plane, X-Y plane, X-Z plane, and isometric views) were produced from the crack tip ROI using the same 1% of control ROI threshold. See Fig. 9.

2.6. Laser scanning confocal and scanning electron microscopy of fracture surfaces

A subset of specimens was also stained with Alizarin Red dye (0.05 mM in ddH_2O) after the $BaSO_4$ staining described above, in order to conduct a qualitative comparative study of the process zone morphology on the X-Y plane between laser scanning confocal microscopy, scanning electron microscopy, and micro-CT. After micro-CT scanning, each specimen was rapidly loaded to complete fracture to expose the two fracture surfaces. These fracture halves were trimmed to a shorter length (2-mm) and mounted on glass microscopy slides in order to place them on the motorized positioning stage of an inverted laser confocal microscope (Nikon C1si, Nikon Instruments Inc., Melville, NY, USA). Using laser confocal microscopy (488 nm excitation; 605 nm emission), stacks of images of the fracture surfaces were generated at 10-μm resolution over a 400-μm depth range. Stacked images were imported into ImageJ (NIH, Bethesda, Maryland, USA) for compiling into 2-D averaged images of the X-Y plane of the fracture surfaces. The same specimens were next prepared for scanning electron microscopy (SEM; XL30 ESEM, Philips, USA; accelerating voltage of 20.0 kV; working distance of 15 mm; spot size 4).

3. Calculations

3.1. Secant modulus method for calculation of P value

Historically, in linear elastic fracture mechanics, the point of crack growth initiation can be detected using a 5% decrease in secant modulus (Anderson, 2005). This is based on the fact that crack growth increases the compliance of the specimen. In elastic-plastic fracture, a non-negligible amount of crack tip blunting and deformation, including micro-damage, can occur before any real crack growth occurs. This increases the apparent compliance of the specimen, resulting in non-linearity in the load vs. load-line displacement curve prior to Pmax. In this study, the percent change in secant modulus during loading (our P value) was calculated using the secant lines as shown in Fig. 2 and used to define progression along the test curve as described above.

3.2. Calculation of J-integral fracture toughness

The J-integral for each specimen at its pre-determined deflection, based on assigned P value, was calculated using the equation prescribed for multi-specimen J_R curves given in (ASTM, 2013):

$$J = \frac{2U}{B(W - a_0)} \ [\mathrm{J/m^2}] \quad (1)$$

where U is the work done to the specimen (area under the load v. load-line deflection curve) up to the prescribed level of deflection, B is the width of the specimen, W is the height and a_0 is the length of the starter notch.

3.3. Micro-damage process zone measurements

3.3.1. Process zone volume

In order to calculate the volume of the stained micro-damage in each specimen's process zone, each thresholded crack tip ROI data set of binary images was stacked and the number of white voxels (corresponding to segmented $BaSO_4$ stained voxels) was counted and the volume was calculated using the 3.57-μm isometric voxel dimensions. Due to small variations in the thickness of the crack tip ROI along the X-axis, the absolute volume of $BaSO_4$ staining (SV) was normalized to the crack tip length as follows:

$$SV_n = SV/l_{ct} \ [\mathrm{mm^3/mm}] \quad (2)$$

where SV was the total volume of stained micro-damage and l_{ct} was the length of the crack tip (along the X-axis).

3.3.2. Process zone dimensions

Process zone width and height were measured on the Y-Z plane. Due to the heterogeneous nature of the micro-damage and staining, filtering and averaging procedures were required. Images were thresholded (as below; Fig. 4A) and consecutive stacks of five images were averaged. A boundary-seeking tool was then used to isolate the largest continuous object in each averaged image. Next, all the boundaries in the stack were averaged, creating an image representative of the average process zone viewed in the Y-Z plane (Fig. 4B). Inevitably, each of these images

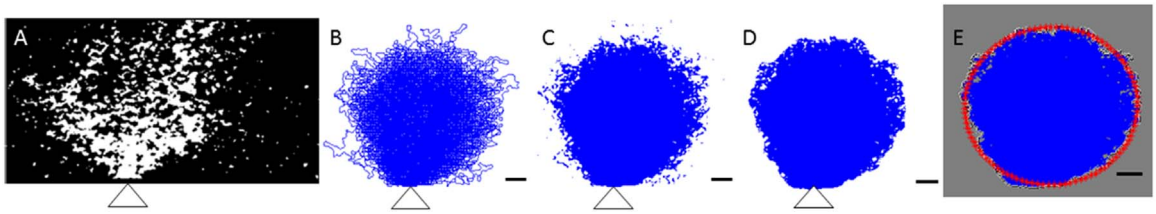

Fig. 4. Demonstration of the image processing steps used for micro-damage process zone dimension measurements. A) Single thresholded image. B) Average of boundaries from five images. C) B despeckled. D) C after outlier removal. E) The ellipse-fitting step, allowing for dimension (width, height) measurements. The black bar is 100 μm in length. The white triangle portrays the location of the crack tip.

contained noise and outliers. These were removed with standard despeckling (Fig. 4C) and outlier removal routines in MatLab (Fig. 4D), resulting in a refined, smoothened image of the through thickness averaged process zone observed on the Y-Z plane. See Fig. 4D.

To each image, an ellipse was fit to the boundary of the process zone using a numerical fitting routine (Fig. 4E) and the lengths of the major (a) and minor (b) semi-axes and their orientation relative to the Y-axis were calculated. The height of the process zone was determined using the ellipse semi-axis with the smallest angle from the Y-axis. The length of this ellipse semi-axis was doubled giving the height in μm when converted from pixels using the 3.57 μm per pixel scale. The width of the process zone was similarly determined using two times the length of the other ellipse semi-axis.

We also conducted verification measurements using the same images (Fig. 4E) but manually making the height and width measurements using NIH ImageJ. Furthermore, since the images processed in this way represent a through-thickness averaging of the 3-D process zone along the X axis, an additional measurement of SV_n, the unit-thickness process zone area projection, was enabled using NIH ImageJ.

3.3.3. Comparison with process zone models

We sought to compare our data with process zone models. Upon examination of the data generated using the methods given above, it was observed that the aspect ratios of the ellipses did not vary greatly from one. Therefore, we started with Irwin's second order estimate of plastic zone radius under plane strain (Eq. (3)) but using the J-based effective stress intensity factor, $K_{IJ} = (E'J)^{1/2}$, in place of K_I (Barthelat and Rabiei, 2011; Anderson, 2005):

$$r_p = \frac{1}{3\pi}\left(\frac{K_I}{\sigma_{YS}}\right)^2 = \frac{1}{3\pi}\left(\frac{E'J}{\sigma_{YS}^2}\right) \text{[mm]} \quad (3)$$

r_p is the radius of the process zone defined by a linear elastic asymptotic stress field in plane strain, K_I is the stress intensity factor, σ_{YS} is the yield strength, E' is the plane strain adjusted Young's modulus, $E' = E/(1-\nu^2)$, where E is the Young's modulus and ν is the Poisson's ratio, and J is the measured J-integral fracture toughness. Values for E, ν and σ_{YS} were estimated (20 GPa, 0.36, 141 MPa respectively) from values reported for bovine cortical bone in bending (Burton et al., 2014; Martin et al., 2015; Willett et al., 2015).

Using r_p, we then calculated the equivalent of the thickness normalized volume of the micro-damage process zone (SV_N) as follows:

$$SV_{n(Irwin)} = \pi r_p^2 \text{ [mm}^2\text{]} \quad (4)$$

This enabled the comparison of experimental data with model predictions over a wide range of J and P values.

3.3.4. Comparison with finite element modeling

The imaged process zone was compared with local stress and strain fields at the notch tip using the commercial finite element analysis software ANSYS (v 15.0, Cannonsburg, PA, USA). The three-point bending test on a bovine cortical bone SENB specimen was simulated. The bone material was assumed to exhibit nonlinear orthotropic stress-strain deformational behavior, and therefore was modeled using a generalized anisotropic Hill's potential theory (Sharma et al., 2012; Shih and Lee, 1978). This theory utilizes Hill's anisotropic yield criterion (Hill, 1983), which accounts for differences in the yield stress for the three main orthogonal directions of the bone (i.e., longitudinal, radial and circumferential), as well as distinct tangent moduli in each direction. Hill's criterion has been found to be effective in modeling cortical bone (Sharma et al., 2012). The model assumes that the post-yield tangent moduli remain constant, and thus bilinear material behavior is considered in each material direction, which is consistent with the observations of (Li et al., 2013). The model also accounts for differences in yield stress in both tension and compression for all material directions, and work hardening as presented by (Valliappan et al., 1976) is used to update the yield criterion. It should be noted that cortical bone does not strictly yield, where instead micro-cracks initiate and grow once a critical stress is attained.

The orthotropic elastic properties of the bone used in the simulation were taken from (Li et al., 2013) and (Bernard et al., 2013), and are presented in Table 1. These were selected because they are consistent with multiple other studies including our own work on bovine cortical bone (Burton et al., 2014; Woodside and Willett, 2016). The yield (critical) stresses and tangent moduli were extracted from the tensile and compressive stress-strain data of (Li et al., 2013), and are shown in Table 2. Since the generalized anisotropic Hill option in ANSYS also requires the shear stress-strain behavior (ANSYS Inc., 2011), it was assumed that the bone will not yield in shear. A small parametric study tested this assumption (data not shown). Our results were unaffected.

The SENB specimen was modeled using 3D solid continuum elements (SOLID 45), which was required in order to capture the plane strain effects. It should be noted that the mesh was refined in the vicinity of the notch tip in order to capture the local stress gradients, as shown in Fig. 5. Two planes of symmetry were defined, thus only a quarter of the edge-notched three-point bending test specimen was modeled (see Fig. 5 top). Symmetric boundary conditions were applied to the two symmetry planes, and a support boundary condition was applied at the lower roller location, which accurately represented the three-point bending testing conditions. The bending load (upper roller) was applied to the finite element model as a line load along the

Table 1
Orthotropic elastic properties of cortical bone used in the simulation (Bernard et al., 2013; Li et al., 2013). Young's moduli (E) and shear moduli (G) in units of GPa, and Poisson's ratios (ν) is dimensionless.

Property	Value
E_{11}	12.8
E_{22}	12.8
E_{33}	20.3
ν_{12}	0.348
ν_{13}	0.275
ν_{23}	0.275
G_{12}	4.8
G_{13}	6.35
G_{23}	6.35

Table 2
Critical stresses (Y) and tangent moduli (E_t) for orthotropic cortical bone used in the simulation, in units of MPa and GPa, respectively (Li et al., 2013). Note that the superscripts denote tension (T) and compression (C).

Property	Value
Y_{11}^T	43
Y_{22}^T	43
Y_{33}^T	90
$E_{t,11}^T$	2.89
$E_{t,22}^T$	–
$E_{t,33}^T$	–
Y_{11}^C	120
Y_{22}^C	120
Y_{33}^C	203
$E_{t,11}^C$	2.68
$E_{t,22}^C$	2.68
$E_{t,33}^C$	3.86

specimen center. A nonlinear solution was required to simulate the quasi-static bending load, and numerical convergence was achieved by using 1000 sub-steps in the solution.

3.3.5. Trend lines and statistical tests

Trend lines were fit using MatLab. Linear and polynomial trends were subsequently confirmed with statistical tests at the 95% confidence level.

4. Results

Of the twenty specimens originally produced for this study, five were removed. Two were removed from the Pmax group because they underwent rapid steady-state fracture before loading was stopped and therefore could not be studied using our methods. One from each of the other groups (P0, P5, P10) was removed either due to excessive porosity leading to over-staining, which created excessive background noise, excessive ring artifacts in the micro-CT reconstruction or, in one case, poor razor notching.

4.1. Pilot studies

Pilot studies were performed to confirm the $BaSO_4$ precipitate distribution and composition. Bright white particulate observed by ESEM-BSE and found in voids were confirmed to be $BaSO_4$ (Fig. 6). Darker regions in the same images lack the multiple Ba and S peaks detected with EDX. Note the heterogeneity of the $BaSO_4$ particles and multiple voids (e.g. lacunae) which were not completely filled with the particulate.

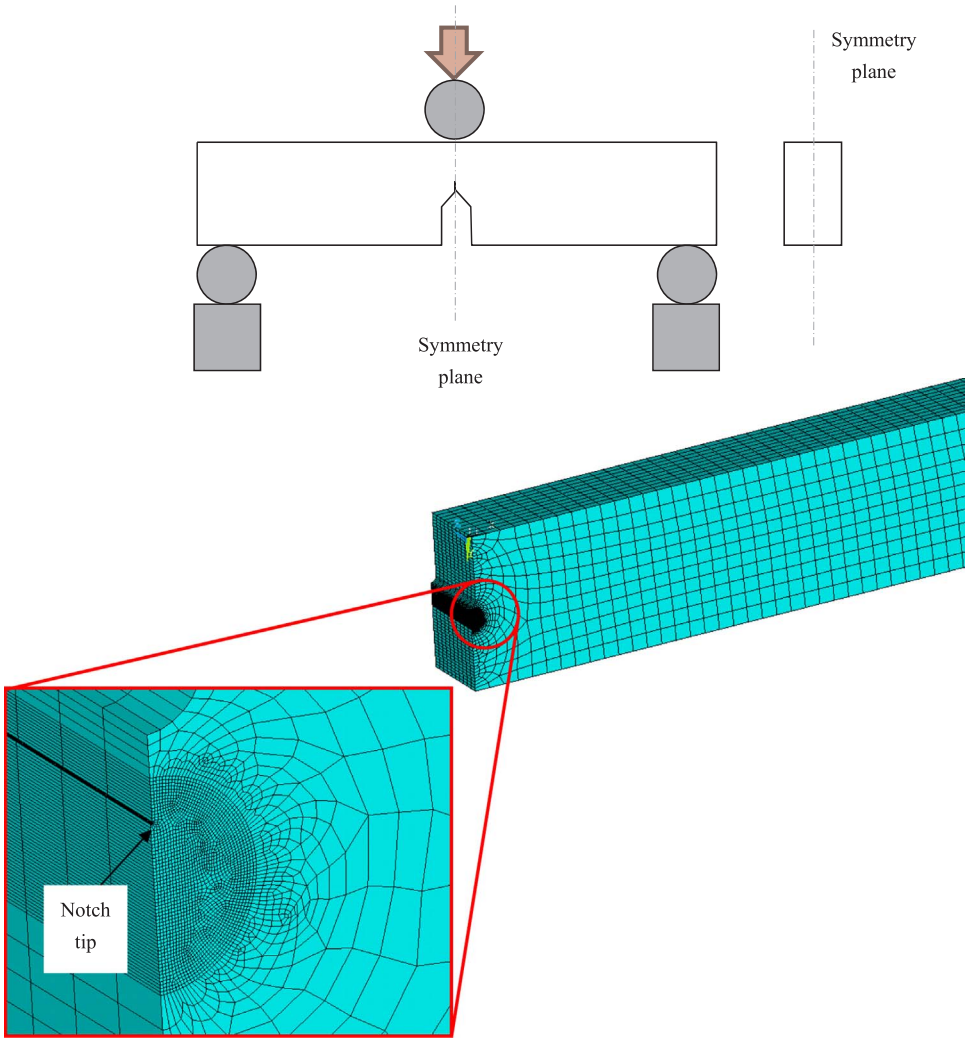

Fig. 5. (top) Geometry of SENB specimen modeled showing symmetry planes and boundary conditions, (bottom) finite element mesh of SENB specimen showing mesh refinement at notch tip.

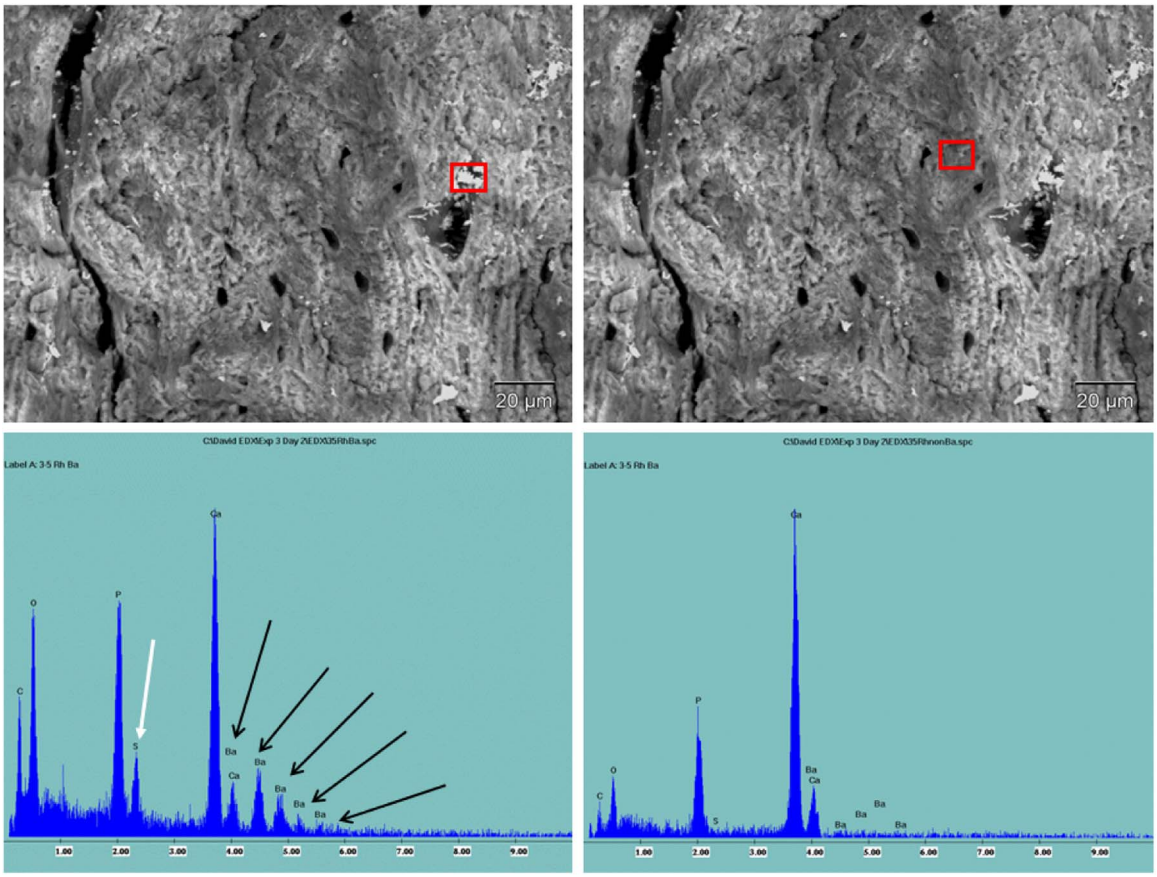

Fig. 6. Observation of $BaSO_4$ distribution in pilot study specimens using BSE-SEM (top left and top right) and EDX confirmation of the composition of the white particles (bottom left and bottom right). Left side images confirm that the bright white particles (within the red box) contain Ba, S and O (arrows in bottom left figure point to Ba (black) and S peaks (white)). (For interpretation of the references to color in this figure legend, the reader is referred to the web version of this article.)

4.2. Mechanical test data

Fig. 7 presents both a representative loading-unloading curve for a P10 specimen (left) and a summary of the P values and paired J values achieved during the experiment (right). Note the non-linear trend in the J versus P data as the irreversible processes contributing to J progress towards steady-state fracture. J is expected to plateau beyond Pmax (Woodside and Willett, 2016).

4.3. Micro-damage zone measurements

Fig. 8 presents the micro-damage process zone dimension measurements (SV_n, width and height; generated by both the pixel counting and projected image approach in the case of SV_n, and ellipse fitting versus manual ImageJ measurements for width and height) versus measured P-values and J values. The volume (and thus Y-Z projected area, SV_n) grew in a non-linear fashion following a second degree polynomial trend ($p < 0.05$). The pixel counting method for determining SV, and thus SV_n, resulted in volume measurements clearly

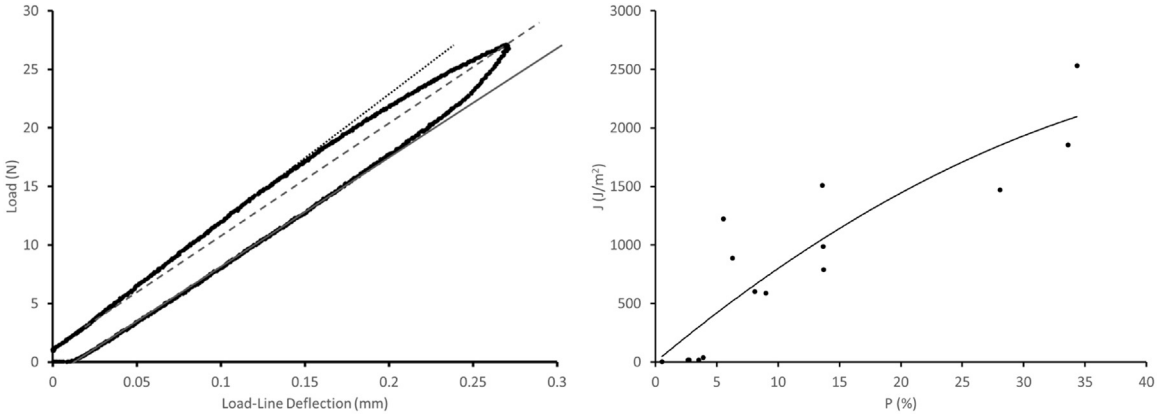

Fig. 7. (Left) An example of load-unload cycle load-displacement data for a P10 specimen, demonstrating a combination of both modulus work and dilatation work. Viscoelastic effects are also apparent. Note the difference in compliance between loading and unloading indicated by changes in the slope of secant lines and the significant hysteresis during the loading-unloading cycle. (Right) Summary of the paired J and P values achieved in the experiment. Note the scatter in the P values around the assigned target values (P0, P5, P10, Pmax) and the scatter in J due to inter-specimen variation in factors including micro-structure, minor preparation variation in notching, for example, and uncontrolled biological variation.

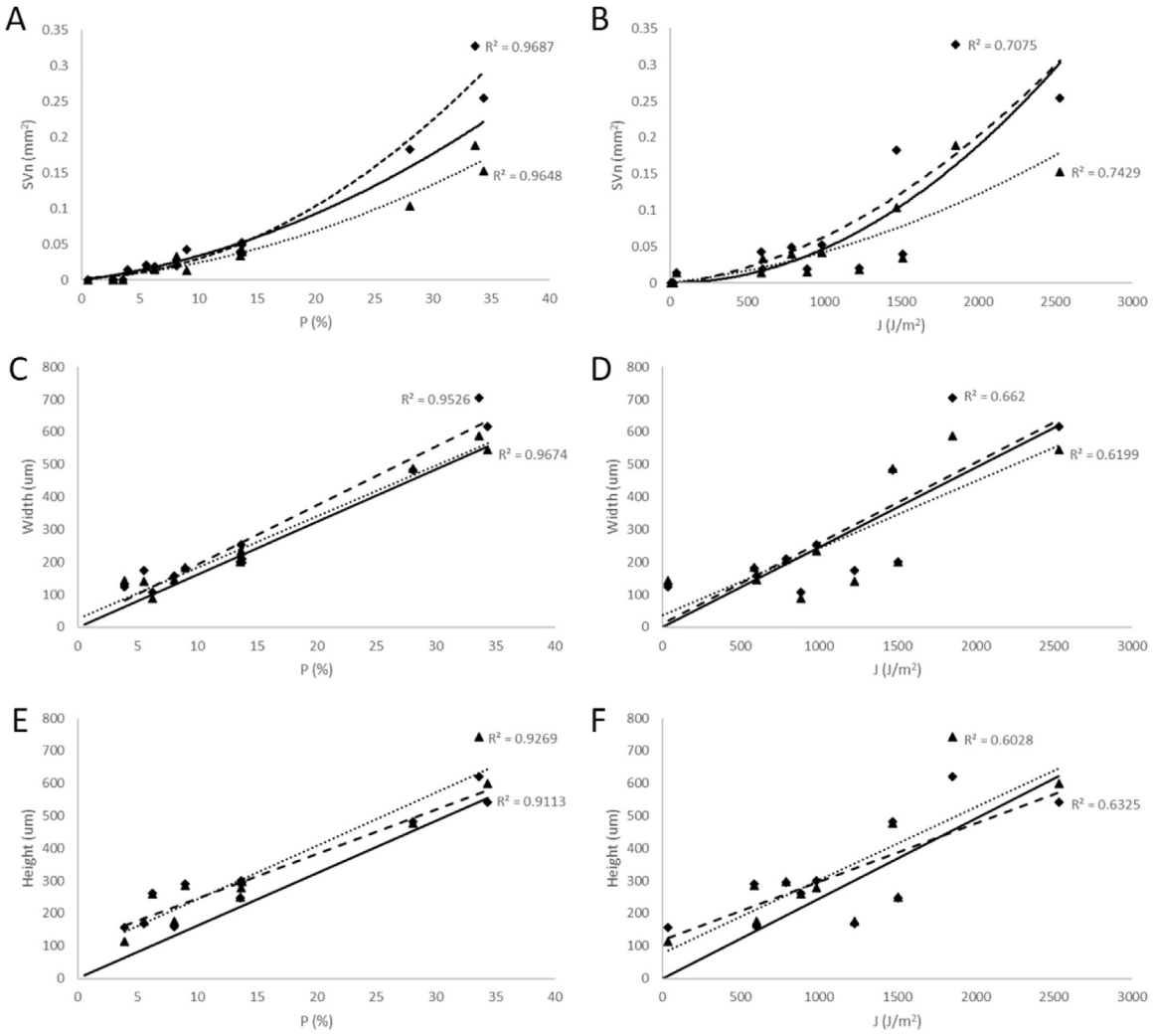

Fig. 8. Micro-damage process zone measurements from micro-CT scans using BaSO4 contrast agent. A) SV_n versus P. B) SV_n versus J. C) Width versus P. D) Width versus J. E) Height versus P. F) Height versus J. Black triangles (▲) in A and B mark the data points generated by the pixel counting method and in C through F, they mark the measurements by ellipse fitting. The fine dotted line marks the corresponding trend line. Black diamonds (♦) in A and B mark the SV_n data points generated by the stacking of images and measurement of the projection onto the Y-Z plane. In C through F, they mark the manual measurements of width and height taken from the same images. The dashed black line marks the corresponding trend line. Finally, the solid black line represents the Irwin model for comparison.

less than those made using the projected image approach. Corresponding to the second order polynomial trend of the volume measurements, both width and height grew according to a linear trend with no indication of an approach to a plateau. The measurements from both methods were similar, depending on whether they were plot versus P or J. Furthermore, in each of the sub-figures in Fig. 8, the Irwin model (solid black line) agrees quite well, falling within the scatter of the experimental data of both methods.

4.4. Qualitative observations of micro-damage process zone morphology

4.4.1. Micro-CT images

At lower P values (P0 and P5), while detectable and measureable, the process zones did not display notable features. By P10, the morphology of a field of micro-damage was evident. Fig. 9A shows an example P10 process zone, which appears to have two lobes on either side of the crack plane along with what appears to be a cohesive tearing zone directly ahead of the tip of the razor notch. By Pmax (Fig. 9C and D), the formation of a large process zone without distinct lobes (or 'ears') was detected in each specimen. In cases with the highest P values, a region of intense staining was observed ahead of the razor notch. This suggests the initiation of true crack growth or a tunneling mechanism. In Fig. 9D, an uneven profile of staining along the X axis is shown, including notable projections of staining jutting ahead of the crack tip. We have termed these features "flames" and they correspond to localized "tunneling" into the microstructure. This phenomenon was also observed in confocal and scanning electron microscopy (Fig. 10).

4.4.2. Microscopy

Using laser scanning confocal microscopy and scanning electron microscopy (SEM), we were able to further examine/confirm some of the features of the process zone in 2-D on the X-Y plane. The features we termed "flames" correspond to localized regions of microstructure between lamellae where the material has broken down, allowing staining with both $BaSO_4$ and Alizarin Red stain, and corresponding to morphology observed in SEM. See Fig. 10.

4.5. Finite element modeling

Non-linear orthotropic finite element models were built to compare the predicted process zone shape with experimental results. Qualitatively, in Fig. 11, the predicted process zone morphology for 28 N (a load corresponding to a P value of approximately 14) is similar to the process zone image in Fig. 10A (a P10 specimen which reached P = 14 and 31 N). Notably, in the finite element model, the cohesive tearing zone is not modeled and a small lobe of material exceeding the

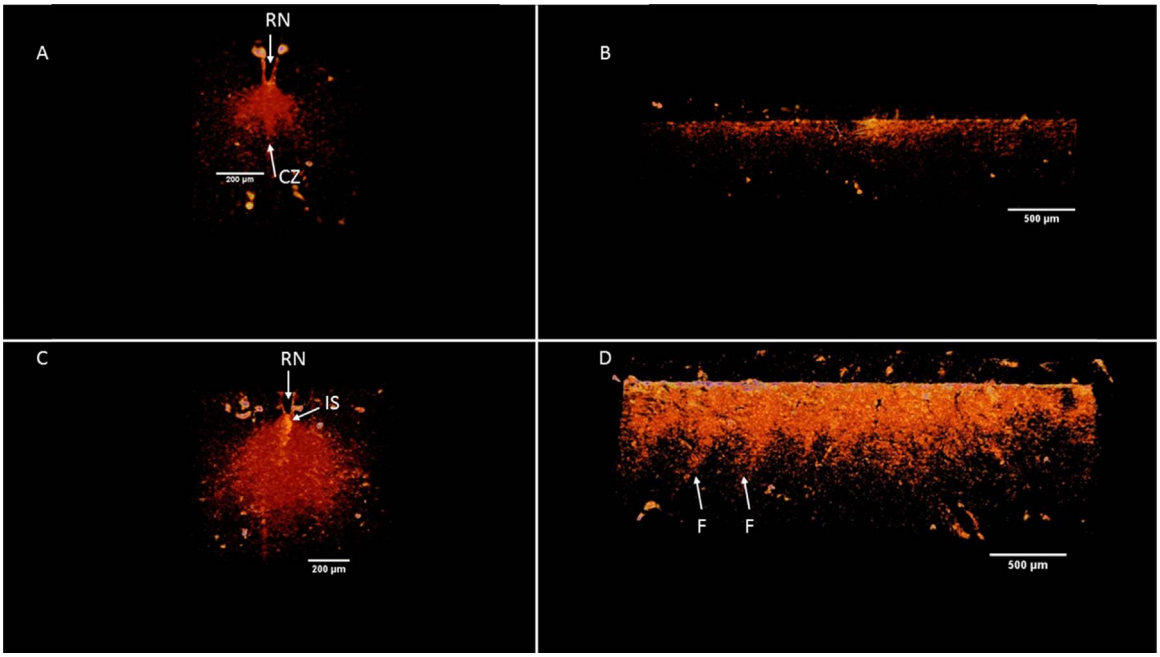

Fig. 9. Representative images of micro-damage process zone from specimens loaded to P10 (A and B) and Pmax (C and D). A and C present Y-Z plane projection views for P10 and Pmax respectively, and B and D present X-Y plane projection views for P10 and Pmax respectively. White arrow labels: RN = razor notch tip, CZ = cohesive zone (tearing), IS = intense staining, F = "flame".

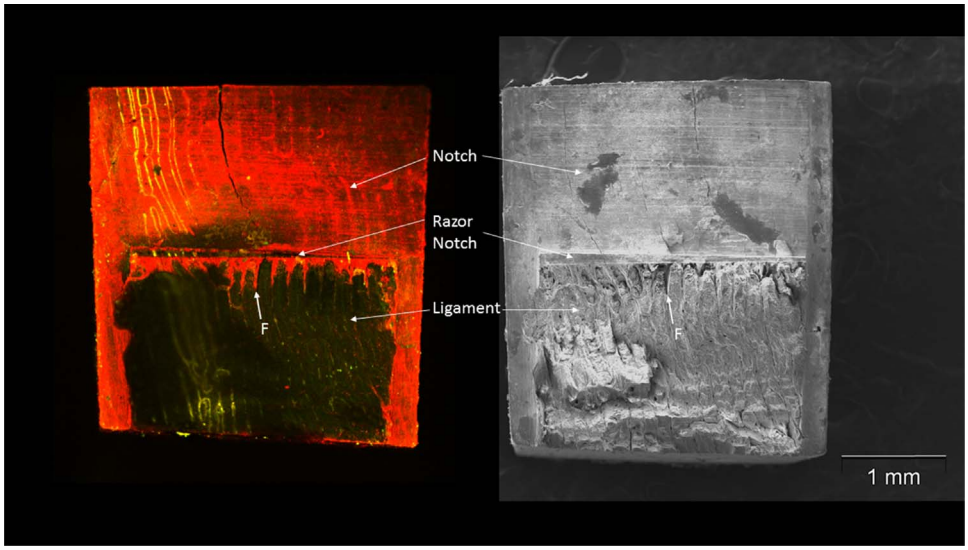

Fig. 10. Microscopy images of a Pmax specimen. (Left) Laser Scanning Confocal Microscopy image of surfaces stained with Alizarin Red. The Alizarin Red binds to exposed mineral surfaces; both cut surfaces from specimen preparation (Notch and Razor Notch) and newly formed crack surfaces ahead of the razor notch (penetrating into the Ligament). (Right) Scanning Electron Microscopy image of the same specimen. Note the paired "flames" (white arrows labeled F in both images). Flames seem to growth into certain regions of inter-lamellar microstructural weakness in Pmax specimens, corresponding to frank crack growth initiation. (For interpretation of the references to color in this figure legend, the reader is referred to the web version of this article.)

Hill's Criterion found behind the starter crack tip is not observed experimentally. Quantitatively, the SV_n predicted by the finite element model (0.0423 mm^3/mm) is similar to the values measured by micro-CT (0.0460 mm^3/mm (stacked images) and 0.0421 mm^3/mm (stained volume)) and predicted by the Irwin's process zone model (0.0498 mm^3/mm).

5. Discussion

To our knowledge, this is the first study to use high-resolution benchtop micro-CT to observe and measure the micro-damage process zone shape and size during transverse fracture testing of cortical bone. Previous studies using similar approaches did not achieve the same level of detail (Burton et al., 2014; Leng et al., 2008). The findings reported herein indicate that an update to textbook information regarding the process zone is in order. Whereas it has been previously assumed that cortical bone under plane strain would display a typical plane strain process zone shape and size with symmetric lobes on either side of the crack plane (Martin et al., 2015), we now know that the process zone is more complicated. The process zone changes and grows and, at maximum load and the initiation of observable crack growth is resembles more closely the plane stress shape previously reported for nacre (Barthelat and Espinosa, 2007; Barthelat and Rabiei, 2011). Furthermore, the micro-damage process zone formation does not reach a steady state prior to or at maximum load during a standard fracture toughness test (Fig. 8) (Vashishth et al., 2003). This is consistent with stable crack growth and rising R-curve behavior. This is also similar to the results reported for nacre (Barthelat and Espinosa, 2007; Barthelat and Rabiei, 2011).

Our measurements are similar in scale to previous 2-D measurements done with histological techniques. (Mitchell et al., 2004), in a study of the effects of radiation sterilization on fatigue crack growth in cortical bone, reported width measurements of the process zone detected histologically. They reported an increasing process zone width

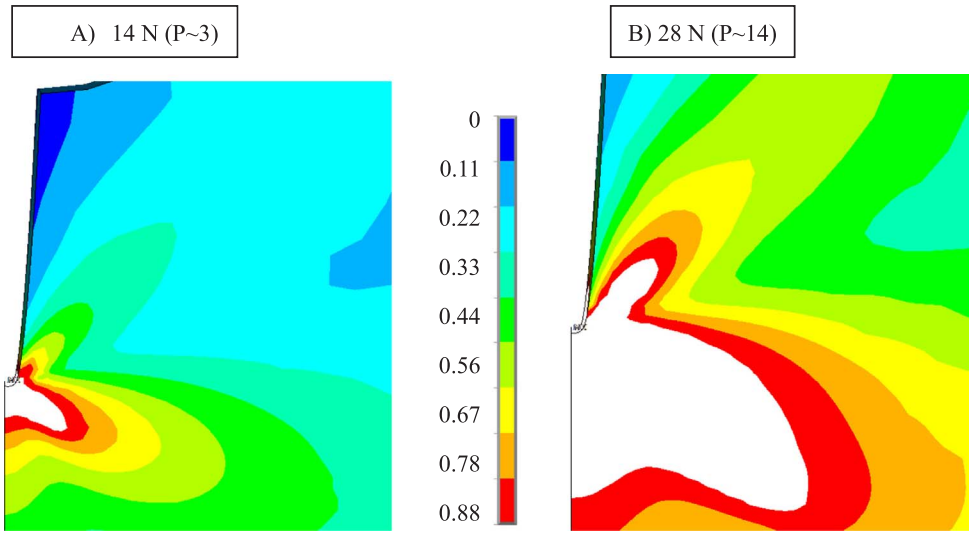

Fig. 11. A) Finite element model of a specimen loaded to 14 N. This corresponds to loading below that experienced by the P0 group. B) Finite element model results for a specimen from the P10 group, loaded to 28 N. These images correspond to the center Y-Z plane of the specimen which experiences plane strain (triaxial stress). The color scale corresponds to the fraction of the Hill's Criterion, i.e. elements exceeding the criterion have the value 1 and are marked in white. (For interpretation of the references to color in this figure legend, the reader is referred to the web version of this article.)

with crack growth and, in normal bone, the width grew up to 200 μm. Interestingly, in irradiated specimens, the width rarely exceeded 100 μm; An effect size due to irradiation similar in magnitude to those we previously reported when using a lower resolution approach similar to the one in this study (Burton et al., 2014). Unfortunately, in (Mitchell et al., 2004), the cracks were propagated in the longitudinal direction (parallel to the osteons), which overlooks the importance of transverse fracture and the higher J-integral fracture toughness measured for transverse fracture (Koester et al., 2011, 2008; Woodside and Willett, 2016; Yan et al., 2007). Also, results for fatigue loading do not compare directly with results from quasi-static fracture toughness tests. Similarly, (Akkus et al., 2000) used histological methods to investigate the diffuse micro-damage associated with the process zone in both transverse and longitudinal crack growth. While they did not report dimensions or morphology of the process zones, their histology suggests diffuse micro-damage formation within a few hundred microns of the fracture plane (i.e. process zone widths of around 500–600 μm) and that the diffuse micro-damage density was approximately an order of magnitude more intense than reported for in vivo Frost-Burr-type micro-crack densities (Akkus et al., 2000).

Our size measurements strengthen previous arguments made in favor of using a J-integral based approach to measuring cortical bone fracture toughness due to the associated specimen size requirements and ability to account for non-linearity in the test curves (ASTM, 2009; Yan et al., 2007; Yang et al., 2006). In our study, the characteristic process zone size at maximum load is approximately 550 μm and smaller than the unbroken ligament thickness (2 mm) and width (4 mm) but larger than allowable for a linear elastic fracture mechanics approach (ASTM, 2009; Yan et al., 2007; Yang et al., 2006). Furthermore, we have found that our process zone dimension measurements agree quite well with a simple, modified Irwin's process zone model, based on a “yielding zone” bounded by a linear elastic singularity field (Anderson, 2005), in which G (elastic energy release rate) was replaced by J (Barthelat and Espinosa, 2007; Barthelat and Rabiei, 2011). This is consistent with cortical bone being a quasi-brittle material toughened by multiple intrinsic mechanisms that act within a defined process zone before crack growth initiation. These multiple mechanisms clearly involve meaningful levels of modulus work and dilation, and indeed viscoelastic/plastic effects (Fig. 7) (Yeni et al., 2007, 2004). They contribute to the meaningful non-linear fracture toughness developed up to maximum load and the onset of frank crack growth (Yan et al., 2007).

In this study, we have also documented an additional mechanism, which we have termed “flames”, due to the morphology observed in micro-CT images (Fig. 9D). These flames may be similar to tunneling observed in other materials during fracture (Anderson, 2005). They occur as the process zone front interacts with the microstructure. Focal sites of micro-damage, and perhaps actual true crack growth, jut out ahead of the body of the process zone at lamellar interfaces. In composites, true crack growth occurs due to intense coalescence of microcracking (Anderson, 2005). This is also the case in cortical bone and thus, it is difficult to determine whether these flames are intense microdamage and/or focal crack growth, even when using a combination of high-resolution micro-CT, laser confocal scanning microscopy and scanning electron microscopy.

As shown in our results, measurement of SV_n depends on the method used. Stained pixel counting within the volume of interest resulted in lower SV_n than the 2-D projection method. The latter effectively generated a through thickness average process zone projected image (Y-Z plane) from which we were able to also make SV_n, width and height measurements. The two methods used to measure width and height resulted in very similar measurements and strengthened our confidence in the use of the projection method for SV_n. Unfortunately, the through thickness average process zone projection method results in a loss of information regarding the variation in the process zone shape through the thickness of the specimen. The fitting of an ellipse to the 2-D projected process zone is an approximation to a more complex morphology but consistent with approaches used for other composite biomaterials, like nacre (Barthelat and Espinosa, 2007; Barthelat and Rabiei, 2011). Additionally, the simple attenuation coefficient-based thresholding approach to distinguish between bone and stain results in some loss of information regarding apparent gradients of staining intensity on the Y-Z plane. The “flame” mechanism was only detected when full process zone reconstructions of specimens loaded to maximum load were viewed in 3-D. In future work, we will adopt more advanced methods in order to preserve more of this information. It will also be fruitful to develop a staining method that results in more homogeneous and consistent staining of micro-damage. Alternatively, in the near future, with the continued development of benchtop micro-CT systems with higher resolution and sensitivity, a truly non-destructive single specimen method may be developed. Such an approach would not require staining with a heavy metal based contrast agent to enable micro-damage detection and could be used in parallel with digital volume correlation (Roberts et al., 2014).

Upon examination of the curves in Fig. 8, one notes that the trend lines against P have much better r-squared values than the trend lines against J. This is partially expected because P was more controlled than J. Recall that each beam was loaded under displacement control to a specified deflection. Tighter correlation with P is also consistent with a fracture process that is strain controlled and dependent upon “post

yield ductility" (Nalla et al., 2003). The J measurements are influenced by inter-specimen variations in microstructure, notching and other uncontrolled biological factors. In our experience, we have found bovine cortical bone to be more consistent in microstructure and quality that human bone, however, it can display a mix of plexiform and osteonal microstructure, lower porosity and other differences that result in fracture behavior that differs from that of human cortical bone. We observed that bovine cortical bone is able to undergo less stable crack growth before steady state fracture than human cortical bone (Woodside and Willett, 2016).

In attempting to understand the shape and size of the micro-damage process zone in our specimens, the experimental tests were conducted to measure the growth of the process zone ahead of the crack tip; however, at this scale, there was no means available to this study to measure the local stress and strain states around the crack tip. Also, due to the complexity of the process zone for cortical bone (i.e., diffuse micro-damage), available analytical models cannot provide accurate predictions of local stress and strain fields. Therefore, a finite element model using modified Hill's theory for the orthotropic bone material was developed to simulate the SENB test. The main goal of the model was to approximate the local stress and strain state near the crack tip in an attempt to provide a means to compare the experimentally measured process zone with the local stress state. These models were built to include the apparent yielding of the material, which is really the critical stress criterion at which micro-cracking starts, and the post-'yield' behavior up to fracture begins. Furthermore, orthotropy was modeled in order to include its effects on the process zone shape. We have demonstrated decent agreement between the normalized stained volume (SV_n) predicted by the models and measured using micro-CT. However, there are distinct differences in process zone morphology between the models and the micro-CT images. This motivates future, more complex studies.

In the finite element models, we selected a yield strength parameter from the lower end of the range typically reported from mechanical testing (90 MPa). The size of the predicted process zone is very sensitive to the yield strength (inverse quadratic relationship) and the post-yield work hardening parameters chosen for the model. Because bone does not yield like metals but rather first micro-cracks, the selection of an appropriate value for yield strength for the models, particularly in the longitudinal direction, is a concern. Choice of a value from the lower end of the typical range was rationalized by the idea that divergence from linear behavior (critical point; proportionality limit), rather than at an arbitrary 0.2% offset strain often used for yield strength determination, is coincident with micro-damage initiation. Selection of 90 MPa in the longitudinal (33) direction resulted in SV_n values comparable to our experimental results, whereas higher yield strength values quickly shrank the process zone to unreasonable values. We also assumed that the bone does not 'yield' under shear. This assumption requires further consideration.

Further work is required to improve the fidelity of our finite element models in terms of determining the best criterion to model the micro-damage process zone. Herein, the focus was not to develop a high fidelity simulation model for predicting bone damage/fracture processes, but instead to complement the experimental results.

6. Conclusion

This study reports details of the fracture process zone previously unreported for cortical bone. This should lead to a better understanding and higher fidelity modeling of the intrinsic fracture toughness of cortical bone in the future. High resolution micro-CT enables 3D visualization and measurement of the process zone and confirmation that the crack front edge and process zone are affected by microstructure. It is clear that the micro-damaged process zone for the specimens studied grows to be meaningfully large (550 μm in diameter), and the process zone does not achieve a steady state by Pmax. Combined with the non-linear loading path to Pmax, these confirm the need for the J-integral approach. With further development, this relatively low-cost benchtop approach (low cost compared with synchrotron instrumentation) may become valuable towards better understanding the role of the process zone in cortical bone fracture and the effects of relevant modifications towards changes in fracture toughness in a cost effective way.

Acknowledgements

Funding: The authors wish to thank the Canadian Institutes of Health Research for research funds awarded to Dr. T. L. Willett.

The authors acknowledge the contributions made by Dr. Marc Grynpas, Mr. Avind John, Mr. Vintoth Tharmakulasingam, Ms. Tutu Udoh-Orok, Mr. Doug Holmyard, Mr. John Georgiou, and Ms. Lisa Yu. The experimental work in this study was conducted in the Musculoskeletal Research Laboratory at the Lunenfeld-Tanenbaum Research Institute of Mount Sinai Hospital (Toronto) with micro-CT scanning conducted in the Mouse Imaging Facility at the Toronto Centre for Phenogenomics.

References

Akkus, O., Jepsen, K.J., Rimnac, C.M., 2000. Microstructural aspects of the fracture process in human cortical bone. J. Mater. Sci. 35, 6065–6074. http://dx.doi.org/10.1023/A:1026719531300.

Anderson, T.L., 2005. Fracture Mechanics: Fundamentals and Applications. CRC Taylor & Francis, Boca Raton.

ANSYS Inc, 2011. ANSYS v15.0 User Manual. Cannonsburg, PA.

ASTM, 2013. Standard test method for determining J-R curves of plastic materials. ASTM Stand. Test Method 1–8. http://dx.doi.org/10.1520/D6068-10.2.

ASTM, 2009. Standard Test Method for Measurement of Fracture Toughness.

Barthelat, F., Espinosa, H.D., 2007. An experimental investigation of deformation and fracture of nacre–mother of pearl. Exp. Mech. 47, 311–324. http://dx.doi.org/10.1007/s11340-007-9040-1.

Barthelat, F., Rabiei, R., 2011. Toughness amplification in natural composites. J. Mech. Phys. Solids 59, 829–840. http://dx.doi.org/10.1016/j.jmps.2011.01.001.

Bernard, S., Grimal, Q., Laugier, P., 2013. Accurate measurement of cortical bone elasticity tensor with resonant ultrasound spectroscopy. J. Mech. Behav. Biomed. Mater. http://dx.doi.org/10.1016/j.jmbbm.2012.09.017.

Burton, B., Gaspar, A., Josey, D., Tupy, J., Grynpas, M.D., Willett, T.L., 2014. Bone embrittlement and collagen modifications due to high-dose gamma-irradiation sterilization. Bone 61, 71–81. http://dx.doi.org/10.1016/j.bone.2014.01.006.

Choudhari, C., Chan, K., Akens, M.K., Whyne, C.M., 2016. μFE models can represent microdamaged regions of healthy and metastatically involved whole vertebrae identified through histology and contrast enhanced μCT imaging. J. Biomech. 49, 1103–1110. http://dx.doi.org/10.1016/j.jbiomech.2016.02.034.

Donahue, S.W., Galley, S.A., 2006. Microdamage in bone: implications for fracture, repair, remodeling, and adaptation. Crit. Rev. Biomed. Eng. 34, 215–271.

Gupta, H.S., Fratzl, P., Kerschnitzki, M., Benecke, G., Wagermaier, W., Kirchner, H.O.K., 2007. Evidence for an elementary process in bone plasticity with an activation enthalpy of 1 eV. J. R. Soc. Interface 4, 277–282. http://dx.doi.org/10.1098/rsif.2006.0172.

Gupta, H.S., Seto, J., Wagermaier, W., Zaslansky, P., Boesecke, P., Fratzl, P., 2006. Cooperative deformation of mineral and collagen in bone at the nanoscale. Proc. Natl. Acad. Sci. 103, 17741–17746. http://dx.doi.org/10.1073/pnas.0604237103.

Hill, R., 1983. The Mathematical Theory of Plasticity. Oxford University Press, New York.

Koester, K.J., Ager 3rd, J.W., Ritchie, R.O., 2008. The true toughness of human cortical bone measured with realistically short cracks. Nat. Mater. 7, 672–677. http://dx.doi.org/10.1038/nmat2221.

Koester, K.J., Barth, H.D., Ritchie, R.O., 2011. Effect of aging on the transverse toughness of human cortical bone: evaluation by R-curves. J. Mech. Behav. Biomed. Mater. 4, 1504–1513. http://dx.doi.org/10.1016/j.jmbbm.2011.05.020.

Landrigan, M.D., Flatley, J.C., Turnbull, T.L., Kruzic, J.J., Ferracane, J.L., Hilton, T.J., Roeder, R.K., 2010. Detection of dentinal cracks using contrast-enhanced micro-computed tomography. J. Mech. Behav. Biomed. Mater. http://dx.doi.org/10.1016/j.jmbbm.2009.10.003.

Landrigan, M.D., Li, J., Turnbull, T.L., Burr, D.B., Niebur, G.L., Roeder, R.K., 2011. Contrast-enhanced micro-computed tomography of fatigue microdamage accumulation in human cortical bone. Bone 48, 443–450. http://dx.doi.org/10.1016/j.bone.2010.10.160.

Launey, M.E., Buehler, M.J., Ritchie, R.O., 2010. On the mechanistic origins of toughness in bone. Annu. Rev. Mater. Res. 40, 25–53.

Leng, H., Wang, X., Ross, R.D., Niebur, G.L., Roeder, R.K., 2008. Micro-computed tomography of fatigue microdamage in cortical bone using a barium sulfate contrast agent. J. Mech. Behav. Biomed. Mater. 1, 68–75. http://dx.doi.org/10.1016/j.jmbbm.2007.06.002.

Li, S., Demirci, E., Silberschmidt, V.V., 2013. Variability and anisotropy of mechanical behavior of cortical bone in tension and compression. J. Mech. Behav. Biomed. Mater. 21, 109–120. http://dx.doi.org/10.1016/j.jmbbm.2013.02.021.

Martin, R.B., Burr, D.B., Sharkey, N.A., Fyhrie, D.P., 2015. Skeletal tissue mechanics. Am. J. Phys. Anthropol. http://dx.doi.org/10.1002/1096-8644(200007)112:3<435::AID-AJPA12>3.3.CO;2-Z.

Mitchell, E.J., Stawarz, A.M., Kayacan, R., Rimnac, C.M., 2004. The effect of gamma radiation sterilization on the fatigue crack propagation resistance of human cortical bone. J. Bone Jt. Surg. Am. 86–A, 2648–2657.

Nalla, R.K., Kinney, J.H., Ritchie, R.O., 2003. Mechanistic fracture criteria for the failure of human cortical bone. Nat. Mater. 2, 164–168. http://dx.doi.org/10.1038/nmat832.

Nalla, R.K., Kruzic, J.J., Kinney, J.H., Ritchie, R.O., 2005. Mechanistic aspects of fracture and R-curve behavior in human cortical bone. Biomaterials 26, 217–231. http://dx.doi.org/10.1016/j.biomaterials.2004.02.017.

Nalla, R.K., Kruzic, J.J., Ritchie, R.O., 2004. On the origin of the toughness of mineralized tissue: microcracking or crack bridging? Bone 34, 790–798. http://dx.doi.org/10.1016/j.bone.2004.02.001.

Poundarik, A.A., Diab, T., Sroga, G.E., Ural, A., Boskey, A.L., Gundberg, C.M., Vashishth, D., 2012. Dilatational band formation in bone. Proc. Natl. Acad. Sci. USA 109, 19178–19183. http://dx.doi.org/10.1073/pnas.1201513109.

Poundarik, A.A., Vashishth, D., 2015. Multiscale imaging of bone microdamage. Connect. Tissue Res. 56, 87–98. http://dx.doi.org/10.3109/03008207.2015.1008133.

Ritchie, R.O., Kinney, J.H., Kruzic, J.J., Nalla, R.K., 2005. A fracture mechanics and mechanistic approach to the failure of cortical bone. Fatigue Fract. Eng. Mater. Struct. 28, 345–371. http://dx.doi.org/10.1111/j.1460-2695.2005.00878.x.

Roberts, B.C., Perilli, E., Reynolds, K.J., 2014. Application of the digital volume correlation technique for the measurement of displacement and strain fields in bone: a literature review. J. Biomech. 47, 923–934. http://dx.doi.org/10.1016/j.jbiomech.2014.01.001.

Sharma, N.K., Sehgal, D.K., Pandey, R.K., Pal, R., 2012. Finite element simulation of cortical bone under different loading and anisotropic yielding situations. Proc. World Congr. Eng. Comput. Sci. II, 22–27.

Shih, C.F., Lee, D., 1978. Further Developments in Anisotropic Plasticity. J. Eng. Mater. Technol. 100, 294. http://dx.doi.org/10.1115/1.3443493.

Sun, X., Hoon Jeon, J., Blendell, J., Akkus, O., 2010. Visualization of a phantom post-yield deformation process in cortical bone. J. Biomech. 43, 1989–1996. http://dx.doi.org/10.1016/j.jbiomech.2010.03.011.

Tang, S.Y., Vashishth, D., 2010. Non-enzymatic glycation alters microdamage formation in human cancellous bone. Bone 46, 148–154. http://dx.doi.org/10.1016/j.bone.2009.09.003.

Taylor, D., Lee, T.C., 2003. Microdamage and mechanical behaviour: predicting failure and remodelling in compact bone. J. Anat. 203, 203–211. http://dx.doi.org/10.1046/j.1469-7580.2003.00194.x.

Turnbull, T.L., Gargac, J.A., Niebur, G.L., Roeder, R.K., 2011. Detection of fatigue microdamage in whole rat femora using contrast-enhanced micro-computed tomography. J. Biomech. 44, 2395–2400. http://dx.doi.org/10.1016/j.jbiomech.2011.06.032.

Valliappan, S., Boonlaulohr, P., Lee, I.K., 1976. Non-linear analysis for anisotropic materials. Int. J. Numer. Methods Eng. 10, 597–606. http://dx.doi.org/10.1002/nme.1620100309.

Vashishth, D., Tanner, K.E., Bonfield, W., 2003. Experimental validation of a microcracking-based toughening mechanism for cortical bone. J. Biomech. 36, 121–124.

Willett, T.L., Burton, B., Woodside, M., Wang, Z., Gaspar, A., Attia, T., 2015. γ-Irradiation sterilized bone strengthened and toughened by ribose pre-treatment. J. Mech. Behav. Biomed. Mater. 44, 147–155.

Woodside, C.M., Willett, T.L., 2016. Elastic-plastic fracture toughness and rising JR-curve behavior of cortical bone is partially protected from irradiation-sterilization-induced degradation by ribose protectant. J. Mech. Behav. Biomed. Mater. 64, 53–64. http://dx.doi.org/10.1016/j.jmbbm.2016.07.001.

Yan, J., Mecholsky, J.J., Clifton, K.B., 2007. How tough is bone? Application of elastic–plastic fracture mechanics to bone. Bone 40, 479–484. http://dx.doi.org/10.1016/j.bone.2006.08.013.

Yang, Q.D., Cox, B.N., Nalla, R.K., Ritchie, R.O., 2006. Re-evaluating the toughness of human cortical bone. Bone 38, 878–887. http://dx.doi.org/10.1016/j.bone.2005.10.014.

Yeni, Y.N., Christopherson, G.T., Turner, A.S., Les, C.M., Fyhrie, D.P., 2004. Apparent viscoelastic anisotropy as measured from nondestructive oscillatory tests can reflect the presence of a flaw in cortical bone. J. Biomed. Mater. Res. 69A, 124–130. http://dx.doi.org/10.1002/jbm.a.20128.

Yeni, Y.N., Shaffer, R.R., Baker, K.C., Dong, X.N., Grimm, M.J., Les, C.M., Fyhrie, D.P., 2007. The effect of yield damage on the viscoelastic properties of cortical bone tissue as measured by dynamic mechanical analysis. J. Biomed. Mater. Res. Part A 82A, 530–537. http://dx.doi.org/10.1002/jbm.a.31169.

Zimmermann, E.A., Schaible, E., Bale, H., Barth, H.D., Tang, S.Y., Reichert, P., Busse, B., Alliston, T., Ager, J.W., Ritchie, R.O., 2011. Age-related changes in the plasticity and toughness of human cortical bone at multiple length scales. Proc. Natl. Acad. Sci. USA 108, 14416–14421. http://dx.doi.org/10.1073/pnas.1107966108.